nature communications



Article

https://doi.org/10.1038/s41467-025-62580-6

Surface chemistry-mediated porewater fluctuations boost CO₂ docking in calcium silicate hydrates

Received: 8 January 2025

Accepted: 24 July 2025

Published online: 11 August 2025

Check for updates

Gen Li¹, Yong Tao $\mathbb{D}^1 \boxtimes$, Yining Gao \mathbb{D}^1 , Roland J.-M. Pellenq \mathbb{D}^2 , Peiliang Shen \mathbb{D}^1 , Xiong Qian¹ & Chi Sun Poon \mathbb{D}^1

While CO₂ mineralization using carbonatable binders and solid waste has become an overwhelming trend in laboratory and industrial trials, a lack of fundamental understanding of the underlying carbonation mechanisms hinders advancement of carbonation technology for large-scale applications. This study addresses this gap by employing Grand Canonical Monte Carlo simulations to unravel the optimal CO₂ sequestration conditions within the mesopores of calcium silicate hydrates, a ubiquitous component of construction materials. Here we show that CO₂-surface interactions dominate at low relative humidity (RH), while CO₂-water interactions prevail at high RH, maximizing CO₂ uptake during capillary condensation, where the metastable porewater boosts CO₂ dissolution. Furthermore, we reveal the influence of surface hydrophilicity on the critical RH for optimal carbonation, indicating that less hydrophilic minerals require higher optimal carbonation RH. These insights into the complex CO₂-water-surface interactions within minerals' mesopores provide a foundation for developing effective CO₂ mineralization strategies and advancing our understanding of geochemical carbonation processes.

To alleviate global warming¹, mainly contributed by excessive carbon emissions², carbon capture and storage technologies have been intensively increasing in the past decades³. Among them, carbon mineralization is developed to effectively utilize the inorganic solid carbonates transformations to fix the anthropogenic CO₂ permanently⁴. This technology originates from the carbonation reactions of Mg and Ca-rich rocks, in which gaseous and dissolved CO₂ are captured and stably stored in carbonate minerals. It is estimated that the CO₂ storage potential of natural ores achieves a scale of gigatons every year⁵. However, due to their inherently low carbonation rate, an extremely high temperature and pressure activation process is always required to drive the reaction, leading to high energy input and cost⁶. On the contrary, each year, gigatons of alkaline solid wastes are generated from activities such as iron/steel production⁷, construction and demolition⁸, coal combustion⁹, etc. The high alkalinity of these

materials enhances their carbonation reactivity and accelerates the kinetics¹⁰, offering a more viable solution for carbon mineralization. More importantly, carbonating these solid wastes not only alleviates their environmental footprints but also promotes material upcycling for a sustainable construction industry. The potential profit is more appealing than many other decarbonization strategies, which are economically unfeasible for large-scale industrial applications. Among a series of alkaline solid wastes, construction and demolition waste is rich in calcium, like calcium hydroxide and calcium silicate hydrates (C-S-H), presenting significant opportunities for CO₂ sequestration and mechanical strengthening through carbonation¹¹.

The carbonation reaction front is believed to be at the solid/liquid interface at the nanoscale, where the nanometer-thick water film adsorbed on the solid surface under specific humidity conditions acts as a nano-reactor for the carbonate precipitation and nucleation¹². For

alkaline materials such as C-S-H, the water film formed on the wall of mesopores performs as the medium for the formation of H₂CO₃. HCO₃-, CO₃²⁻ species as well as interlayer Ca²⁺ dissolution, significantly controlling carbonation reactions¹³. On the other hand, the infiltration and diffusion of CO₂ within these pores play a pivotal role in reactant supply, which governs the entire CO₂ mineralization efficiency in practical applications¹⁴. Experimental studies have extensively focused on the C-S-H carbonations¹⁵, pointing out the critical role of Ca/Si ratio and relative humidity (RH) in influencing carbonation thermodynamics and kinetics^{16,17}. C-S-H with a higher Ca/Si ratio typically acquires a faster carbonation reaction for its high dissolution rate¹⁸. Optimal water content constructs a suitable water-saturated porous system, enhancing the CO₂ diffusion in voids and solid grains¹⁹. However, the carbonation enhancement of thin water film can diverge drastically when confined to nanoscale pores (<10 nm)¹² due to the constitutive behaviors of water film under such dimensions often defying its macroscopic description²⁰. Therefore, the mechanism of water content affecting CO₂ docking in C-S-H remains controversial. The thermodynamics of thin water film is highly affected by solidliquid interactions²¹, which is motivated by solid surface properties. Hence, critical research gaps are exposed to demonstrate the impact of solid-liquid-gas interactions on CO2 docking in hydrophilic mesoporous minerals.

In this work, we focus on C-S-H, the most important CO₂-reactive minerals in global construction and demolition wastes that hold gigatons of CO₂ removal capacity, to investigate its surface propertyregulated CO2 adsorption behavior using the advanced Grand Canonical Monte Carlo (GCMC) method. The optimal CO₂ adsorption capacity is observed within the C-S-H gel pores at a critical water content, corresponding to the metastable water layer at the onset of capillary condensation. More importantly, the critical water content for capillary condensation is found to be regulated by the surface charges and texture, which are related to the Ca/Si ratio of C-S-H. A more hydrophilic surface with a lower Ca/Si ratio necessitates a lower water content for optimal CO₂ adsorption. This study reveals the nanoscale mechanisms by which the interfacial properties of alkaline minerals influence maximum CO2 uptake. It provides fundamental guidelines for efficient CO2 sequestration through accelerated mineralization.

Results

Optimal humidity for CO₂ adsorption

The stacking voids in between C-S-H nanograins store nanometer-thick water films under varying RH prior to local capillary condensation²², which perform as nano-reactors for carbonation²³. The water film thickness and state are highly dependent on the surface properties of C-S-H, which are controlled by the Ca/Si ratio. CO2 adsorption and transport in these nanometer-thick environments critically influence carbonation efficiency. Experimental investigations typically apply a constant environmental RH to keep the equilibrium moisture content of the minerals during carbonation. Therefore, we delicately controlled the water content within the C-S-H pores, mimicking the different RH environments, to simulate its impact on CO2 adsorption. Here, the split pore models (referred to as nanochannels) of C-S-H are constructed to reproduce the CO2 adsorption process. Slit pore models have been widely utilized to investigate small molecule adsorptions in porous media from both simulation $^{24-26}$ and theoretical aspects²⁷ (see Supplementary Note 6). Such models provide simple and effective insights in simplifying the complicated pore structure

Figure 1a and Supplementary Fig. 1a–c exhibit the total CO_2 adsorption amount in C-S-H nanochannels for varying RH and Ca/Si ratios. Generally speaking, the CO_2 adsorption amount increases with water content, indicating that the higher water film thickness benefits partial CO_2 solvation. The highest CO_2 adsorption amount is reached

when RH reaches 0.46-0.54. However, when the water coverage density exceeds a critical value, the CO₂ adsorption amount sharply decreases to a very low value. Under very high-water coverage conditions, the nanochannel is filled with liquid water, leaving little space for CO₂ diffusion. Thus, the adsorption efficiency is highly limited. Figure 1b shows the total (dissolved and gaseous) CO₂ intake as a function of water saturation degree for different C-S-H slit pores. The water saturation degree is defined as the ratio of the water amount to the maximum amount that fills up the entire pore. Figure 1c further classifies the dissolved CO₂ into fully dissolved and interfacially dissolved CO₂ based on their water coordination numbers (see Supplementary Note 4). When the water saturation degree is no greater than 0.5, with the increase of water film thickness, the dissolved CO₂ amount gradually increases while the interfacial CO₂ amount remains stable. The dissolved CO2 amount barely changes when the water film is thick enough (water saturation degree >0.5), indicating the same solubility of CO₂ under varying RH. The fully dissolved CO₂ amount is expected in theory to be comparable to the condition of water saturation degree of 0.87. The apparently lower CO₂ amount is due to the slow CO₂ diffusion kinetics in liquid water, which requires further increase of simulation time to reach its dissolution limits. Based on Fig. 1a-c, the two-fold effect of the Ca/Si ratio on CO2 adsorption in the C-S-H nanochannel is observed. Under low water coverage density (water saturation degree <0.5), a high Ca/Si ratio acquires high CO₂ adsorption capacity. However, the CO₂ adsorption capacity under high-water coverage density becomes more complicated. The C-S-Hs with Ca/Si ratios of 1.2, 1.5, and 1.8 reach the maximum CO_2 intake at RH = 0.46, 0.48, and 0.54, respectively. It is interesting to observe that these critical water contents all correspond to a transition state of the pore water at the onset of water capillary condensation (Fig. 1f).

Taking the water state in C-S-H with the Ca/Si ratio of 1.8 as an example, the pore water exists as the layered water film on the C-S-H pore wall at low RH (Fig. 1d), whereas it suddenly saturates the entire mesopore (Fig. 1e) when the RH reaches 0.54. The layered water refers to the stable liquid water state with a density of ~1 g/cm³. The condensed water exhibits a metastable condition (transition state), where the density of the water is lower than that of normal bulk water (1 g/ cm³), as theorized by Saam and Cole²⁸. Based on the oscillatory mode of helium at low temperatures, they proposed a universal theory to describe the metastable state of liquids at capillary condensation within confined porous media, which was later successfully adopted by Keizer et al.²⁹ to investigate the phase transition of sulfur hexafluoride in controlled-pore glass using molecular simulations and experiments. In our simulations, we observed that the C-S-H pore appears filled with liquid water at the onset of capillary condensation, yet the actual water content is slightly lower than the theoretical volume required for complete pore filling. This incomplete filling with barely discernible air voids results in a lower average water density within the pore compared to the fully saturated state (bulk water density). For more discussion on the low-density water at capillary condensation, please consult Supplementary Note 1.

The critical water film thickness to activate capillary condensation has been discussed in the literature through the f/d ratio, where f is the maximum thickness of the stable water film prior to capillary condensation and d is the split pore width³⁰. The theoretical value of f/d is -0.3, subject to variation based on the material properties³¹. This indicates that the maximum water content that remains stable in the capillary pore is -60%. Figure 1g-i demonstrates that water condensation occurs when RH reaches 0.46, 0.48, and 0.54 in C-S-H slit pores with Ca/Si ratios of 1.2, 1.5, and 1.8, respectively. This result indicates that C-S-H pores with a higher Ca/Si ratio necessitate a larger RH to trigger capillary condensation, which is the optimal condition for maximum CO₂ intake, as exhibited in Fig. 1f. The synergistic effects of water content and Ca/Si ratio intricately influence not only CO₂ adsorption but also the phase transition of pore water. Subsequent

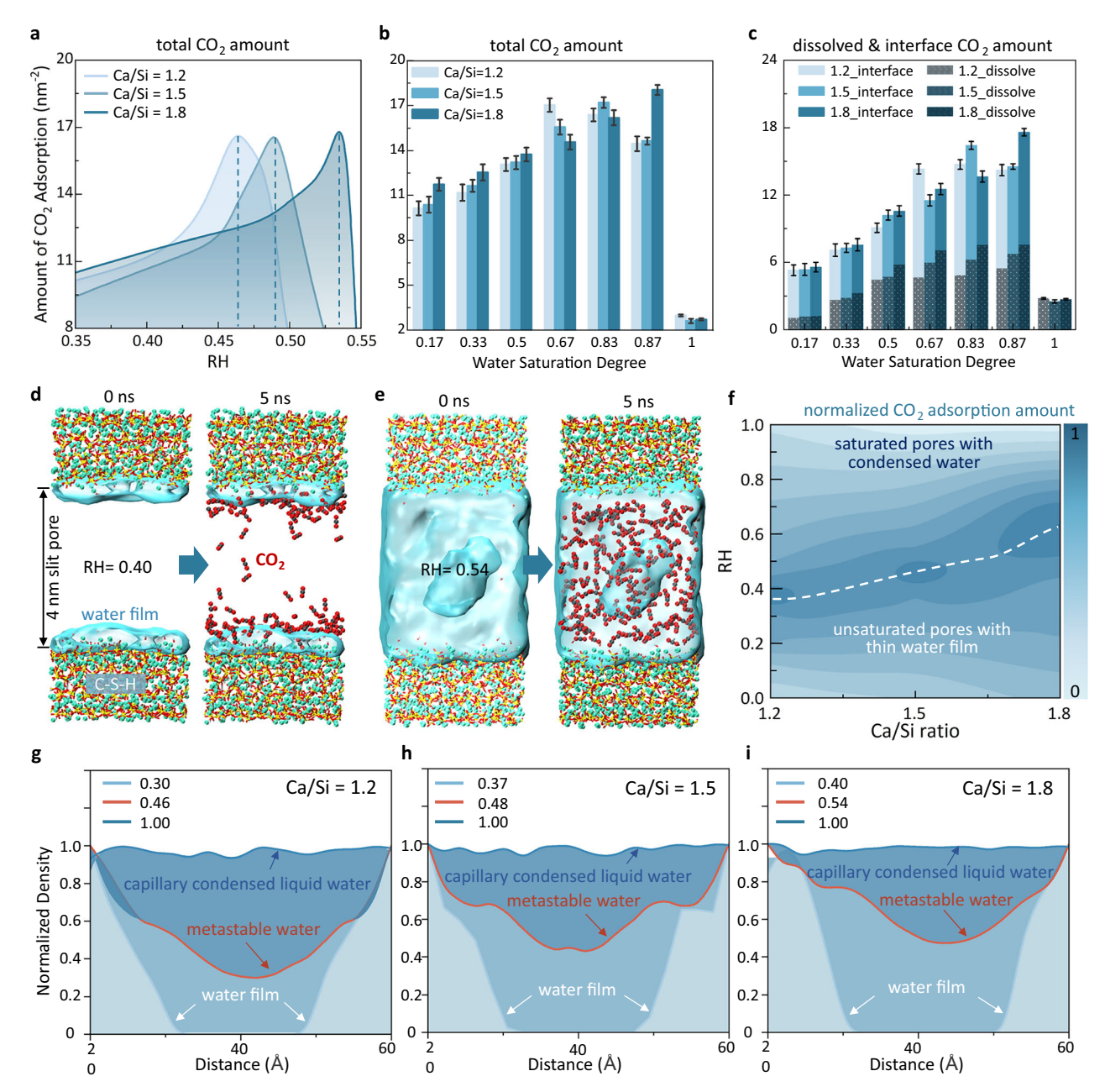


Fig. 1 | ${\rm CO_2}$ adsorption in 4 nm C-S-H slit pores under different RHs. a Effect of RH on the total ${\rm CO_2}$ amount in C-S-H slit pores with different Ca/Si ratios. **b** Effect of water saturation degree on the total (dissolved and gaseous) ${\rm CO_2}$ amount for different C-S-H slit pores. **c** Further classification of fully dissolved and interfacially dissolved ${\rm CO_2}$ amount based on their water coordination numbers (see Supplementary Note 4). The water saturation degree is defined as the ratio of the water amount to the maximum amount that fills up the entire pore. Error bars are from the standard deviation resulting from the last 1 ns simulation of ${\rm CO_2}$ adsorption. The unit is the number of molecules. **d**, **e** Molecular simulation snapshots showing

CO $_2$ adsorption into the C-S-H (Ca/Si=1.8) pores at RH=0.40 and 0.54, respectively. These images were generated using Visual Molecular Dynamics software 61 . f Normalized CO $_2$ adsorption capacity as a function of RH and Ca/Si ratios of C-S-H. The white dashed line outlines the onset of pore water condensation states, below and above which are the unsaturated pore with an adsorbed water film and the fully saturated pore, respectively. g-i Water density distributions along the Z direction of the C-S-H nanochannels with varying Ca/Si ratios at different RHs. Red lines show the water density distribution at the critical RHs where capillary condensation initiates. Source data are provided as a Source Data file.

sections will delve deeper into the surface effects on CO_2 adsorption and water phase transformation within C-S-H mesopores by answering three questions: why the C-S-H with a higher Ca/Si ratio possesses a higher CO_2 adsorption amount, why maximum CO_2 intake occurs at the capillary condensation states, and why the capillary condensation happens at a lower RH for C-S-H with a lower Ca/Si ratio.

Water-mediated CO₂-surface interactions

To answer the first and second questions, two key factors influencing CO₂ adsorption in mesoporous media should be addressed: the solid-

gas³² and liquid-gas interactions³³. The former mainly contributes to CO_2 adsorption in dry conditions, while the latter facilitates CO_2 dissolution in pore solutions when surface water is thick enough at higher RH prior to the water capillary transition. Both interactions are dominated by surface texture and electrical properties. Surface water film acts as a dielectric barrier and attenuates CO_2 -surface interactions. This electrostatic shielding effect is directly related to the dielectric constant (ε_r) of adsorbed/confined water, which varies in different C-S-H systems and reflects the strength of the electrostatic interaction between the water film and solid surfaces. It is interesting to observe

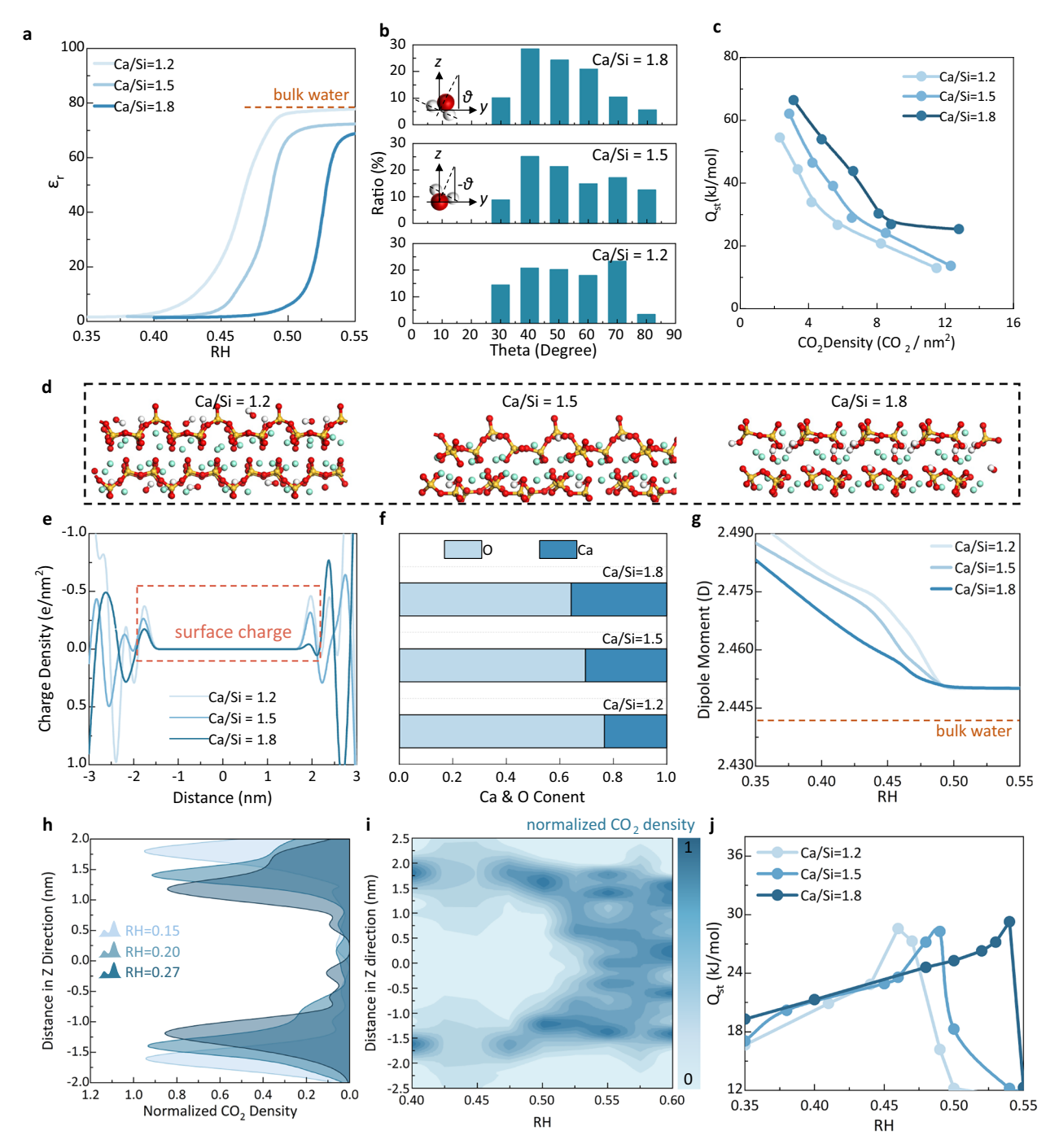


Fig. 2 | **Surface-water-CO₂** interactions and their impact on **CO₂** adsorption. a Dielectric constants of the water film as a function of RH in different C-S-H pores. The dashed line indicates the experimental dielectric constant of bulk water 62 . b Water molecule orientation in C-S-H slit pores. The orientation angle (θ) is calculated as the angle between the symmetry axis of water molecules and the C-S-H surface. c Isosteric heat of CO₂ adsorption in different C-S-H pores with a water saturation degree of 0.17. The water saturation degree is defined as the ratio of the water amount to the maximum amount that fills up the entire pore. d Surface textures of C-S-H with different Ca/Si ratios. The red, white, yellow, and cyan

spheres represent oxygen, hydrogen, silicon, and calcium atoms, respectively. These images were generated using Visual Molecular Dynamics software 61 . $\mathbf e$ Surface charge distributions of C-S-H with different Ca/Si ratios. $\mathbf f$ Ca/O ratios on different C-S-H surfaces. $\mathbf g$ Water dipole moment as a function of RH in different C-S-H pores. The dashed line indicates the experimental dipole moment of bulk water 63 . $\mathbf h$ CO₂ distribution along Z distance in the C-S-H pore (Ca/Si = 1.8) at low RHs. $\mathbf i$ CO₂ distribution along Z distance in the C-S-H pore (Ca/Si = 1.8) at different RHs. $\mathbf j$ Effect of RH on isosteric heat of CO₂ adsorption in different C-S-H pores. Source data are provided as a Source Data file.

that with the increase of the Ca/Si ratio, a lower ε_r is observed (Fig. 2a), indicating a weaker electrostatic shielding effect. This can be attributed to the differences in C-S-H surface texture. C-S-H with a higher Ca/Si ratio exhibits more surface defects (Fig. 2d), facilitating the entrapment of water molecules in confined environments, leading to a more ordered dipole moment orientation distribution. Consequently,

the water orientation distribution in C-S-H with a Ca/Si ratio of 1.8 is more centered, whereas it is more evenly distributed in C-S-H with a Ca/Si ratio of 1.2 (Fig. 2b). The ordered arrangement of water molecules finally leads to a lower dielectric constant. The dielectric constant of the surface water film shows its potential to weaken the interactions between the solid surface and $\rm CO_2$ molecules, which could be

described in a dielectric continuum view by $E_{ij}^{\rm disp-corr} = E_{ij}^{\rm disp}/\epsilon_r^2$ as the dominating term in the water-mediated CO₂/surface potential is the dispersion interaction term (the electrostatic quadrupolar CO₂/surface contribution is of smaller magnitude as the CO₂ quadrupole moment is small and writes $E_{ij}^{\rm elect-corr} = E_{ij}^{\rm elect}/\epsilon_r$). It should be noted that this scaling relation is used here only as a conceptual framework to explain the shielding effect of the surface water layer. We did not apply this equation to modify the force field parameters or the Coulombic interactions in our atomistic simulations because the dielectric screening effects are inherently captured through explicit water molecules. Such empirical scaling might be appropriate in coarsegrained or continuum models where water is treated as a simplified continuum dielectric. Therefore, at low RH, the less pronounced shielding effect of the water film on high-Ca/Si-ratio C-S-H explains its larger CO₂ adsorption capacity (Fig. 1a, b).

To quantify the surface-CO $_2$ interactions at low RH conditions, the isosteric heat of CO $_2$ adsorption ($Q_{\rm st}$) was calculated from fluctuations in internal energy and the adsorbed quantity of CO $_2^{26}$. $Q_{\rm st}$ represents the heat released per unit of CO $_2$ adsorbed, indicating the stability of CO $_2$ adsorption. We calculated $Q_{\rm st}$ of equilibrium CO $_2$ adsorption at different CO $_2$ gaseous pressures under low RH conditions where water is adsorbed on the pore walls to form thin water films (Fig. 2c). The CO $_2$ adsorption amount increases with the gas pressure as expected (Supplementary Fig. 3). The gradual increment of CO $_2$ adsorption amount results in the decrease of $Q_{\rm st}$ (Fig. 2c). This is because the accumulated CO $_2$ molecules have weaker interactions with the solid surface than the first adsorption monolayer, causing a decrease in the average $Q_{\rm st}$ of adsorbed CO $_2$ molecules. The higher Ca/Si ratio always leads to higher $Q_{\rm st}$, which indicates stronger surface-water-CO $_2$ interactions, resulting in a larger CO $_2$ adsorption amount.

Besides the different shielding effects of surface water film on surface-CO₂ attractions that impact CO₂ adsorption, the difference in CO₂ solvation ability of C-S-H surface water also leads to different CO₂ intake, which is related to the surface charges (see Supplementary Note 8). It is observed that C-S-H with a higher Ca/Si ratio acquires a lower surface charge density (Fig. 2e). As the Ca/Si ratio increases, the silicate chain becomes more defective due to the depletion of bridging silicate tetrahedra, leading to a larger diffusion of inner intralayer Ca ions into the surface silicate chain layer (Supplementary Fig. 13). This process elevates the Ca/O ratio on the C-S-H surface (Fig. 2f), resulting in a reduction of surface negative charges (Fig. 2e). This observation aligns with experimental conclusions derived from zeta potential testing³⁴. Due to the negative charges on the C-S-H surfaces, most CO₂ molecules are horizontally adsorbed on the surface so that their positive centers (carbon atoms) are more closely attracted to the surface (Supplementary Fig. 2). Similarly, this negatively charged surface significantly influences the water film structure by attracting hydrogen atoms while repelling oxygen atoms. This behavior alters the bond lengths and angles of water molecules, leading to the enhanced polarization of the water film compared to bulk water (Fig. 2g). With increasing RH, the dipole moment of water in all C-S-H models decreases and approaches that of bulk water. This occurs because the accumulating water layers further from the C-S-H surface are less affected by the surface charge. C-S-H with lower Ca/Si ratios exhibits higher surface charge densities, leading to increased polarization of the water molecules, as reflected by their enhanced average dipole moment (Fig. 2g). The highly polarized surface water depresses the solubility of the non-polar CO₂ molecules, thus accounts for the reduction of dissolved CO₂ amount in C-S-H with low a Ca/Si ratio (Fig. 1c). Previous study on calcium silicate minerals has confirmed that the enhanced polarization of surface water would limit the CO₂ dissolution²⁵.

Predominant CO₂-water interactions

With the increase in water film thickness, the surface-CO₂ interaction sharply shrinks. In such conditions, the surface-adsorbed water film

becomes the dominant CO₂ sink where the water-CO₂ interactions rule the CO₂ adsorption capacity. The abrupt increases in ε_r of pore water (Fig. 2a) coincide with the RH values at which capillary condensation occurs within the C-S-H pores (Fig. 1g-i). At these RH levels, the strong dielectric screening effect of water renders surface-CO2 interactions negligible, and CO₂ adsorption is therefore primarily driven by water-CO₂ interactions. As illustrated in Fig. 2h and Supplementary Fig. 4, CO₂ molecules favor positioning at the water/CO₂ interface, which confirms the predominant impact of gas-liquid interactions on CO2 adsorption. The liquid/gas interface exhibits the lowest free energy, providing the most stable environment for CO₂ docking³⁵. At the onset of capillary condensation, metastable pore water forms numerous gasliquid interfaces and leads to more violent liquid-gas interactions than the water film at low RH, thereby significantly intensifying its CO₂ storage capacity. The diffusion coefficient of adsorbed CO2 sharply decreases at this moment (Supplementary Fig. 5) due to the suddenly increased water density hindering CO2 molecules' movement. The increased number of water molecules interacting with CO2 leads to stronger CO₂-water interactions, limiting the dynamics of CO₂. Above the critical RH of capillary condensation, the adsorbed CO2 molecules are homogeneously distributed in the entire pore (Fig. 2i). The liquid/ gas interfaces totally disappeared so that CO₂ adsorption is ruled by the limited CO₂ solubility in bulk-like water, leading to a sharp decrease in CO2 adsorption capacity. The entire RH-dependent CO2-water interactions are quantified by the calculated $Q_{\rm st}$ (Fig. 2j). With the increase of RH, Q_{st} gradually increases and reaches the maximum value when water capillary condensation occurs, after which it suddenly drops to the lowest.

Hydrophilicity-driven water condensation

Figure 1g-i shows that C-S-H mesopores with Ca/Si ratios of 1.2, 1.5, and 1.8 reach their condensation states at the critical RHs of 0.46, 0.48, and 0.54, respectively. This discrepancy indicates that the surface properties influence water phase transformation within C-S-H mesopores. More specifically, when RH = 0.46, water condensation is achieved in the C-S-H slit pore of Ca/Si ratio = 1.2, while the Ca/Si ratio = 1.5 mesopore exhibits water bridges. In contrast, under the same RH, the pore water in C-S-H with a Ca/Si ratio of 1.8 remains a stable surface film. To further uncover the underlying mechanism, we compared the surface potential between water molecules and different C-S-H surfaces. Figure 3a presents the C-S-H surface potential to a single water molecule. The growth of the Ca/Si ratio largely reduces the surface attraction, implying that C-S-H with a lower Ca/Si ratio exhibits much higher attraction to water molecules. Taking the system of Ca/Si ratio = 1.8 as an example, the oxygen ion in water molecules (Ow) is repulsed by the C-S-H surface due to the Coulombic repulsive potential being stronger than Lennard-Jones attractive potential (Fig. 3b). On the contrary, the hydrogen atoms in water molecules (Hw) are strongly attracted by the negatively charged C-S-H surface, thereby exhibiting a closer distance with C-S-H surface compared to O_w species (Fig. 3f). The water molecule orientation distribution (Fig. 2b) also provides identical results that most water molecules exhibit a positive orientation angle, indicating H_w tends to be closer with the C-S-H surfaces. The water isosteric heat of adsorption also shows stronger hydrophilic behaviors of low-Ca/Si-ratio C-S-H (Fig. 3c). The $Q_{\rm st}$ of single water molecule adsorption for Ca/Si ratios 1.2, 1.5, and 1.8 are ~82, 70, and 62 kJ/mol, respectively, which is comparable with previous studies^{26,36}. $Q_{\rm sr}$ gradually decreases to a low value (-10 kJ/mol) as the water adsorption amount increases, which is due to the reduced interactions between the solid surface and accumulated water molecules. The $Q_{\rm st}$ value reflects the energy associated with the adsorption process, that is, the sum of the water-surface and water-water interactions. To evaluate the $Q_{\rm st}$ of bulk liquid water, we constructed an empty box $(30 \times 30 \times 30 \text{ Å}^3)$ to adsorb liquid-state water using the GCMC method and calculated its Q_{st} evolution. The Q_{st} of bulk liquid water is -3 kJ/mol

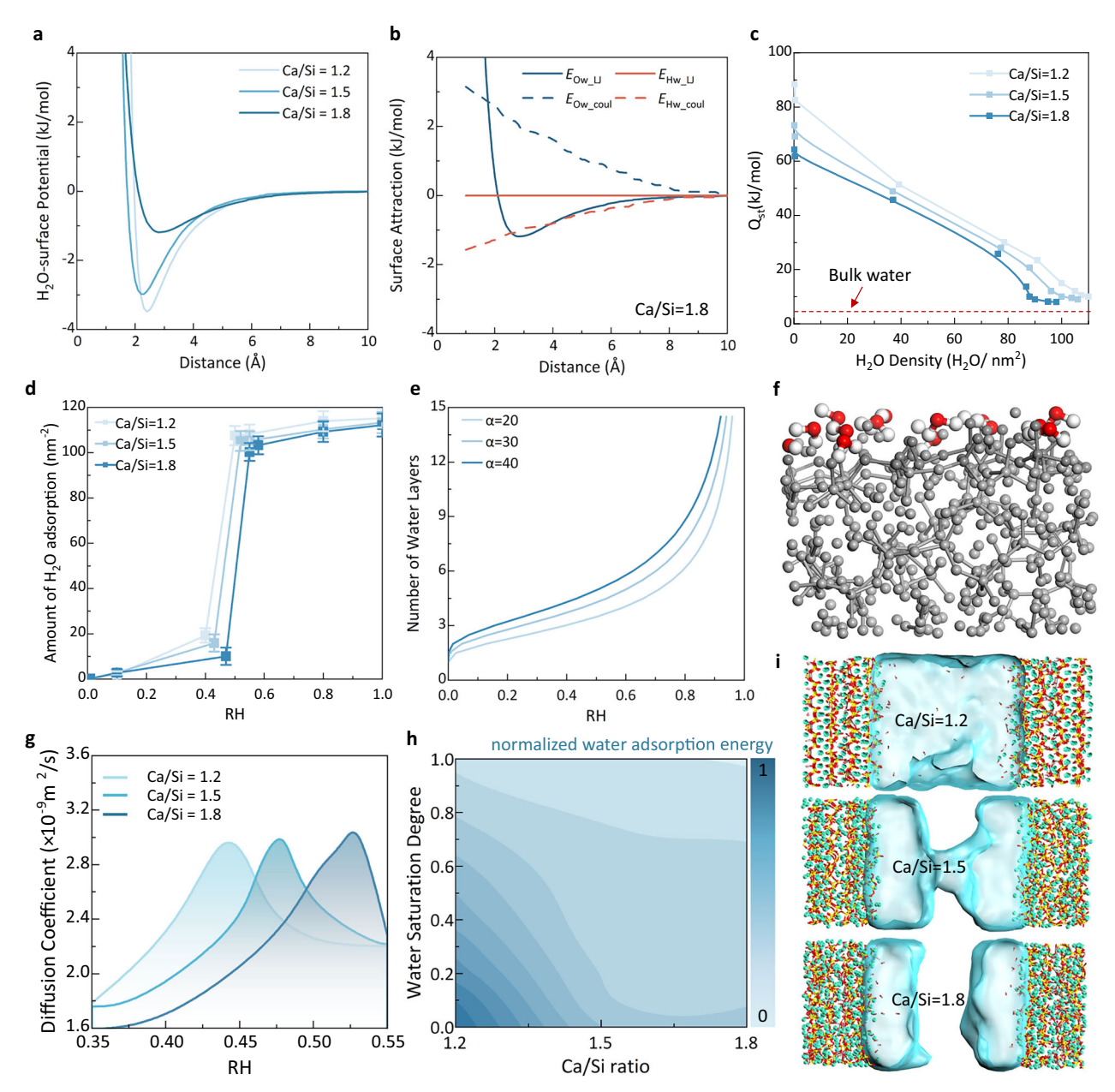


Fig. 3 | **Surface-water interactions and their impact on water condensation. a** H₂O-surface potentials as a function of distance for different C-S-Hs. **b** Lennard-Jones potentials and Coulombic potentials of O and H in a single H₂O molecule with respect to the C-S-H surface (Ca/Si = 1.8). **c** $Q_{\rm st}$ of H₂O adsorption on C-S-H surfaces with varying Ca/Si ratios. The dashed line indicates the $Q_{\rm st}$ of bulk water calculated with a water box of $30 \times 30 \times 30$ Å³. **d** Water sorption isotherms for different C-S-Hs. Error bars are from the standard deviation resulting from the last 1 ns simulation of H₂O adsorption. The unit is the number of molecules. **e** Accumulative surface water layers with the increase in RH predicted by the Frenkel–Halsey–Hill Equation^{37,64}. A larger surface adsorption energy (α) leads to a thicker adsorbed water layer. **f** Molecular simulation snapshots showing water molecules adsorbed on the C-S-H surface. The H atoms in H₂O molecules are oriented to the C-S-H

surface due to the negative surface charges. **g** Water diffusion coefficients in C-S-H pores at different RH conditions. Due to the size effect of finite systems on the simulation of self-diffusion coefficients, the calculated results are slightly underestimated (see Supplementary Method). It does not influence the comparison of the different C-S-H systems as they have the same model size. **h** Effect of Ca/Si ratios and water saturation degrees on water adsorption energy. The adsorption energy is normalized with the maximum of absolute values. The water saturation degree is defined as the ratio of the water amount to the maximum amount that fills up the entire pore. **i** Molecular simulation snapshots showing water states in different C-S-H pores at the RH of 0.46. These images were generated using Visual Molecular Dynamics software⁶¹. Source data are provided as a Source Data file.

(Fig. 3c), which is slightly lower than the $Q_{\rm st}$ observed for condensed water in the fully saturated C-S-H mesopores. This discrepancy arises from the enhanced water–surface interactions that facilitate water adsorption in the C-S-H matrix.

As observed from surface potentials and $Q_{\rm st}$ low-Ca/Si-ratio C-S-Hs exhibit a more hydrophilic surface. Therefore, more water could be adsorbed into the low-Ca/Si ratio-C-S-H nanochannel at the same RH, leading to the earlier initiation of water capillary condensation

(Fig. 3d). Similar results could be found through the Frenkel-Halsey-Hill equation³⁷, which describes the water layer thickness in the slits under varying RH. The material-related parameters highly affect the accumulative water layer thickness on the materials' surface, as the larger surface adsorption energy (α) leads to the thicker water layer (Fig. 3e). When the surface water film is sufficiently thin, it experiences negligible interaction with the opposing pore wall due to the large separation distance. As the film thickens, its upper layers approach the

opposite wall, progressively sensing stronger intermolecular attractions. This interaction eventually leads to capillary condensation of water within the pore. In this regard, a more hydrophilic surface. meaning stronger water-surface affinity, requires a lower water content to initiate capillary condensation. In the C-S-H system, a lower Ca/ Si ratio leads to an increase in water adsorption energy (Fig. 3h and Supplementary Fig. 6), thereby necessitating less water content to trigger water condensation (Fig. 3i). The influence of hydrophilicity on pore water phase behavior is further supported by the variation in water diffusion coefficients at different RH (Fig. 3g). In the direction perpendicular to the surface, water molecules located closer to the C-S-H surface experience stronger surface attraction, which restricts their mobility and results in lower self-diffusion coefficients. As the distance from the surface increases, the influence of surface interactions diminishes, and the diffusivity correspondingly increases. At the vapor-liquid interface, water molecules exhibit the highest mobility due to the minimal constraints, leading to the highest local diffusion coefficients. While it is challenging to compute the self-diffusion coefficient for each individual water layer with high accuracy, we instead analyze the average self-diffusion coefficient of the surface water film as a function of its thickness under various RH conditions. At low RH, the C-S-H system with a lower Ca/Si ratio exhibits larger hydrophilicity, resulting in thicker surface water films (Fig. 3e). These thicker films include water layers further from the surface, which contributes to a higher average self-diffusion coefficient (Fig. 3g). As RH increases and capillary condensation occurs, the active water molecules at the vapor-liquid interface disappear abruptly, and the confined pore water recovers a bulk-like state. This transition leads to a drop in the average diffusion coefficient to values closer to those of bulk water. C-S-H with a lower Ca/Si ratio undergoes capillary condensation at a lower RH, causing this drop in diffusivity to occur earlier compared to systems with higher Ca/Si ratios.

Discussion

Calcium-bearing minerals such as calcium oxide and calcium silicates can, in principle, directly react with CO₂ to form calcium carbonate through a surface-mediated pathway. This pathway typically involves surface adsorption of CO₂, CO₂ speciation into CO₃²⁻, and subsequent in-situ nucleation and growth of CaCO₃. However, due to the relatively high energy barriers associated with CO₂ speciation and CaCO₃ nucleation on dry solid-gas interfaces, such reactions generally require elevated temperatures or mechanical activation to proceed efficiently³⁸. In contrast, minerals containing structural

hydroxyl groups, such as portlandite, undergo carbonation more readily at the solid-gas interface. The presence of surface hydroxyl groups facilitates CO₂ speciation by lowering the activation energy, making carbonation of portlandite more kinetically favorable. Nevertheless, even in this case, solid-gas interface reactions remain limited by slow proton transfer and atomic rearrangement, which can constrain the overall efficiency of CO₂ mineralization. Compared to these dry pathways, the introduction of water fundamentally alters the reaction mechanism by establishing a solid-liquid-gas threephase interface. This transition effectively shifts the reaction environment into the aqueous phase, significantly lowering the energy barriers for ion migration, CO₂ speciation, and CaCO₃ nucleation and growth. As such, water-mediated carbonation has become the predominant focus of both experimental and computational studies in CO₂ mineralization³⁹⁻⁴¹. The water-mediated mechanism typically involves five key steps: CO₂ adsorption, Ca²⁺ dissolution, CO₂ speciation, CaCO₃ complexation, and nucleation/growth. Variations in water content and state under different RH conditions within mineral mesopores can critically influence each of these steps. Among them, CO₂ physisorption reaches equilibrium rapidly, which is the first step followed by a series of slower, non-equilibrium reactive steps that face substantial free energy barriers 42,43. While our future work will address these complex reactive steps, the current study focuses on evaluating how nanoconfined water content affects the equilibrium CO2 adsorption capacity, serving as the CO2 reservoir size within mineral mesopores (see Supplementary Note 5). This is a crucial factor that determines the local concentration of reactants available for downstream reactions and ultimately governs the kinetics and efficiency of mineral carbonation. Our previous study on portlandite established a basic engineering model to predict the optimal RH for CO₂ uptake, which involves a material-specific factor²⁴. In this work, we extend that framework to C-S-H, a more structurally complex alkaline solid waste system, to reveal how surface structures and chemistry modulate nanoconfined water states, which in turn control CO₂ adsorption behavior. Since the surface structures and chemical properties of C-S-H are directly determined by the Ca/Si ratio by regulating the silicate chain length, the CO₂ adsorption behavior within the C-S-H pore is thus correlated to the Ca/Si ratio (Fig. 4).

Under the low water coverage conditions, the gas-solid interaction rules the CO_2 adsorption amount within the pore, while the dielectric properties of the water film serve as a shielding effect on the gas-solid interaction. A higher Ca/Si ratio of C-S-H results in a smaller dielectric constant of the surface water film due to the more defective

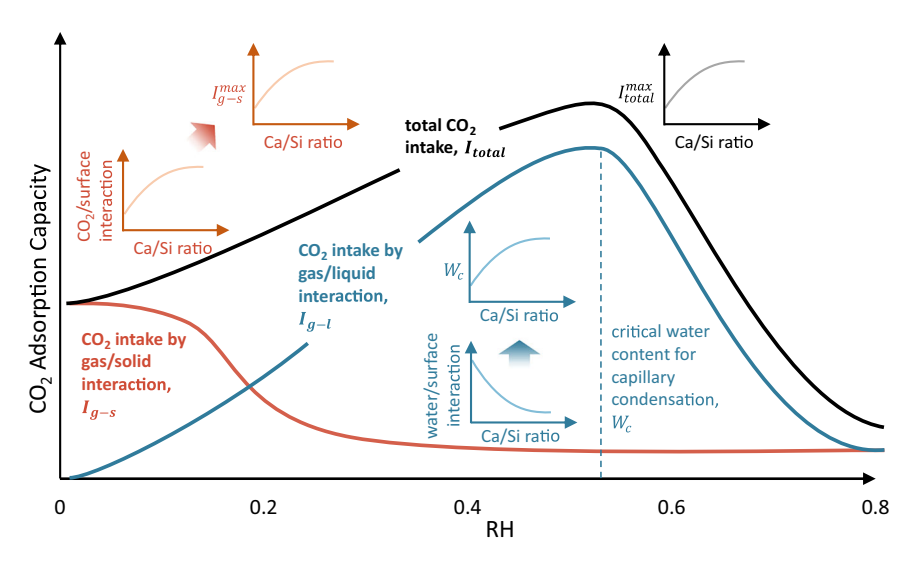


Fig. 4 | Schematic demonstration of water content and Ca/Si ratio-dependent CO_2 adsorption in C-S-H mesopores. The Ca/Si ratio-dependent surface properties control the strength of gas/solid (I_{g-s}) and gas/liquid interactions (I_{g-l}) , while the water content rules the contribution rates of them to the CO_2 adsorption capacity.

surface texture, which leads to a weaker shielding effect on the gassolid interactions. This causes enhanced CO₂ adsorption with an increased Ca/Si ratio. Under high-water content conditions, the gasliquid interaction becomes the determining factor for CO₂ adsorption. with a maximum intake achieved during capillary condensation, where the density-fluctuating pore water significantly intensifies the gasliquid interfacial interactions. Therefore, achieving this critical state of pore water by precise control of the external water supply is imperative for improving CO₂ mineralization in experiments and industrial applications. Moreover, it is interesting to observe that capillary condensation within the C-S-H pore is delayed with an increased Ca/Si ratio, suggesting that C-S-H with a higher Ca/Si ratio requires a larger water amount to attain the optimal carbonation condition. This phenomenon is fundamentally governed by water-surface attractions, where a higher Ca/Si ratio of C-S-H exhibits a weaker surface attraction to water molecules, resulting in a less hydrophilic surface. These comprehensive insights into CO₂-water-surface interactions within mineral mesopores advance our ability to control CO₂ mineralization kinetics and deepen the understanding of geochemical carbonation processes. Building on these findings, we plan to investigate more complex systems, such as multiphase and polydisperse environments, in order to develop a more robust and generalized predictive model. This will provide theoretical guidance for scaling up CO₂ mineralization technologies utilizing carbonatable industrial wastes and natural minerals.

Methods

Model construction

The C-S-H models used in this study were constructed based on the 11 Å tobermorite with a Ca/Si ratio of 1.044. Starting from an orthorhombic 11 Å tobermorite unit cell by redefining the lattice, supercell models were constructed (Supplementary Fig. 7). The C-S-H models with the Ca/Si ratio of 1.2, 1.5, and 1.8 were built by carefully removing the bridging silicate monomers $(SiO_2)^{45-47}$, in which process the Q_n factors of these models follow the realistic C-S-H characteristics determined by Si²⁹ NMR^{48,49}. Then, a reactive force field (ReaxFF)⁵⁰ was used to reproduce the reaction between interlayer water and silicate sheets. In this process, the reaction between interlayer water molecules and silicate chains could be reproduced to form Si-OH groups and OH⁻ ions. ReaxFF has been widely used in simulating the reactions in silicate minerals⁵¹, especially describing the bond formation and breakage in hydro-reactions⁵². The atom charges were calculated during the ReaxFF simulations using the charge equilibration method^{53,54}. The supercells were relaxed for 6 ns at 300 K and 1 bar under NPT ensembles to reach the equilibrium of silicate chains' protonation/deprotonation, after which the models were further relaxed with the C-S-H force field (CSH-FF)55 for 1 ns under NPT ensembles. All parameters are provided in Supplementary Tables 1 and 2. Based on the atom charges calculated by ReaxFF, we specified the charges of each atom type according to the CSH-FF framework⁴⁷ to ensure they remain within suggested ranges by the force field. After full relaxation, the C-S-H surface models were built with a 4 nm slit pore (Supplementary Fig. 7c). Water films were put on both sides of the C-S-H pore walls. Different water contents were considered to build the C-S-H mesopores with different water saturation degrees. A 12 Å cutoff distance is utilized, higher than which the non-bonded interactions are ignored. In this condition, the water capillary condensation is influenced by the water film thickness. The relation between water content and RH was derived through a series of water adsorption tests (see Supplementary Note 7). Finally, the water-saturated models were relaxed again with CSH-FF under NPT ensembles for 1 ns, in which three diagonal components were coupled. All simulations in this work were conducted with LAMMPS⁵⁰ software. The Nose-Hoover barostat and thermostat were used for constant pressure and temperature control. The integration timesteps for CSH-FF and ReaxFF⁵¹ simulations were set as 1 fs and 0.2 fs, respectively. For the treatment of long-range electrostatics, we employed the standard Ewald method with full 3D periodicity due to the model consisting of two C-S-H slabs forming a slit pore of 4 nm in width, with water and ions confined in between. This configuration is designed to represent a realistic interlayer or interparticle environment within cementitious materials, rather than a single isolated surface exposed to vacuum. We did not use the slab correction option for the 3D Ewald method, as it is specifically designed to eliminate spurious interactions in systems with single-surface geometries and artificial vacuum spacing in the non-periodic direction⁵². Applying such a correction in our case would artificially suppress the electrostatic interactions between the two physically meaningful confining surfaces, which are central to the behavior of the confined aqueous phase.

CO₂ and water adsorption process

CSH-FF was utilized in the entire CO_2 and water adsorption processes, in which the parameters of CO_2 molecules were obtained from Cygan et al's work⁵⁵. GCMC methods were employed to reproduce the CO_2 adsorption in C-S-H mesopores with different water saturation degrees. GCMC provides a solution to exchange species in a simulation box with the pre-defined reservoirs so that CO_2 molecules can be inserted, moved, or removed in C-S-H mesopores, which allows us to mimic the CO_2 adsorption in wet C-S-H mesopores. The chemical potential of CO_2 adsorption reflects the equilibrium state of CO_2 in a confined system, which also highly affects the CO_2 adsorption amount. The chemical potential of CO_2 under ambient conditions of atmospheric pressure (1 bar) and room temperature (300 K) is -40 kJ/mol. The variation of chemical potential in other pressure conditions can be calculated by

$$\mu = \mu_0 + RT \ln \frac{p}{p_0} \tag{1}$$

where μ_0 and p_0 represent the chemical potential and pressure under ambient conditions, respectively. The amount of CO2 adsorption increases with the gas pressure, i.e., chemical potential. A CO2 pressure of 10 bars was selected following preliminary adsorption tests to ensure a sufficient number of CO2 molecules for statistical analysis and to maintain a pressure comparable to that utilized in carbonation experiments (see Supplementary Note 2). In the simulation procedure, we used a timestep of 1 fs, and CO₂ molecules were cyclically absorbed, desorbed, or moved 100 times every 10 ps, and the entire system was relaxed for another 10 ps. The CO₂ adsorption continued for 8 ns to reach the equilibrium state, with 8 million Monte Carlo moves to ensure the convergence of the CO₂ amount in the reservoir (see Supplementary Note 3). The configuration-biased Monte Carlo probability was set as 0.125, with a maximum rotation of 0.05 rad and a maximum displacement of 0.5 Å. In the entire simulation process, the trajectories of all atoms were recorded every 10 ps for further analysis. The amount of adsorbed CO₂ is obtained every 1 ps, and the total CO2 adsorption amount is calculated from the average CO₂ amount in the last 1 ns after the adsorption reaches equilibrium. The standard deviation in these periods is computed as the error bar.

As for the water adsorption, we adopted the saturated vapor pressure of $4.4\,\mathrm{kPa}$ for SPC water⁵⁶. The corresponding chemical potential of SPC water under saturated pressure and $300\,\mathrm{K}$ is $-46\,\mathrm{kJ/mol^{21}}$. The configuration-biased Monte Carlo probability was set as 0.25, while other parameters are all the same as in $\mathrm{CO_2}$ adsorption. The water vapor pressure was changed to evaluate the total amount of adsorbed water under the RH ranging from 10% to 100%. Each adsorption process contained at least 5 million Monte Carlo steps to ensure the equilibrium state is achieved.

Surface attraction of C-S-H

The atomic charges of the C-S-H slit pore systems were calculated using the ReaxFF⁵⁷. The surface attraction potentials of C-S-H with respect to H₂O molecules were calculated based on the Lennard-Jones ($E_{\rm Bi}$) and Coulombic ($E_{\rm coul}$) potentials by

$$E_{ij} = 4\varepsilon_{ij} \left[\left(\frac{\sigma}{r} \right)^{12} - \left(\frac{\sigma}{r} \right)^{6} \right]$$
 (2)

$$E_{\text{coul}} = \frac{Cq_1q_2}{\varepsilon_r r} \tag{3}$$

where ε_{ij} and σ represent the usual Lennard-Jones potential parameters. C, ε_r =1 and q_{ij} are energy-conversion constant, dielectric constant, and charges of the paired atoms, respectively. Here, we assume a H₂O molecule is placed at the center of the C-S-H surface (Supplementary Fig. 8). Then, the selected molecule was gradually moved away from the C-S-H surface vertically, during which Lennard-Jones and Coulombic potentials were calculated to obtain the total surface attraction of C-S-H to the H₂O molecule. The distance cutoff for the vertical displacement of the H₂O molecule was set at 12 Å.

Isosteric heat of adsorption

The adsorption isotherms of CO_2 and water molecules are obtained by the average number of adsorbed molecules as a function of the pressure of the gas reservoir. Based on the saturated vapor pressure of water and CO_2 at $300\,\mathrm{K}^{36,58}$, the chemical potential μ is changed to reach the varying adsorption quantity, and the deduced p/p_0 can be obtained from Eq. (1) according to the bulk equation of state for an ideal gas. The calculated μ_{CO_2} and μ_{H_2O} and the deduced p/p_0 can be found in Supplementary Tables 3 and 4. Here, the total energy of the equilibrium system of adsorbate/substrate is computed under varying μ after energy minimization. The isosteric heat of adsorption (Q_{st}) is then computed by

$$Q_{\rm st} = RT - \frac{(\langle UN \rangle - \langle U \rangle \langle N \rangle)}{\left(\left\langle N^2 \right\rangle - \langle N \rangle^2\right)} \tag{4}$$

where R and T are the universal perfect gas constant and temperature, U and N represent the energy fluctuation and adsorbed quantity, respectively.

Diffusion coefficient

The diffusion coefficients (D) of water and CO_2 molecules are calculated through the mean square displacement (MSD) according to their trajectories as

$$D = \frac{\text{MSD}(t)}{6\Delta t} \tag{5}$$

where Δt is the time interval. The periodic boundary conditions influence the self-diffusion coefficient, caused by the altered hydrodynamic interactions between particles in a periodic system⁵⁹. To evaluate the system-size-independent self-diffusion coefficient in C-S-H with PBC structures, we referred to the work done by Yel and Hummer⁶⁰, which could directly calculate the error between corrected and uncorrected diffusion coefficient through the formula: $k_B T \xi / 6 \pi \eta L$, where $\xi \approx 2.837297$, k_B is the Boltzmann constant, T is the absolute temperature, and η is the shear viscosity of the solvent. The induced errors could be estimated through a linear relationship between D_{PBC} and the inverse of box length L (Supplementary Fig. 10a). Based on their findings, we calculated the error in our diffusion coefficient according to the size of the slit geometry to be -11% lower, which is acceptable within our simulation results.

The determination of time difference (Δt) for calculating the diffusion coefficient is critical as the self-diffusion coefficient should be

assessed in the region where a linear behavior is observed in the log-log plot of MSD versus time. Therefore, we used a water box sized $25 \times 25 \times 25$ ų to calculate the MSD of the system after full relaxation. The log-log plot of MSD versus time was analyzed (Supplementary Fig. 10b–g). We found that when the time interval is less than 6 ps, the linear behavior is not well fitted, while a clear linear trend is observed for time intervals greater than 6 ps. Thus, we selected 6 ps as our time interval for calculating MSD.

Dialectical constant

To calculate the dielectric constant (ε_r) of surface water, the dipole moment (\mathbf{M}) of the surface water film is determined from

$$\mathbf{M} = \sum q \mathbf{d} \tag{6}$$

where **d** represents the displacement vector from the negative to the positive charge, and q denotes the charge. The total dipole moment is calculated by summing the contributions from each water molecule adsorbed on the C-S-H surface. Following this, the system is fully relaxed using the NPT ensemble at 300 K and 1 bar for 1 ns. The NVT ensemble is then applied at 300 K to record the trajectories of the water molecules over a period of 2 ns, during which the dipole moment is computed every 1 ps. Finally, the mean value and variance of the dipole moment are calculated, which allows for the estimation of the dielectric constant through

$$\varepsilon_{\rm r} = 1 + \frac{\text{Var}[\mathbf{M}]}{3\varepsilon_0 V k_{\rm B} T} \tag{7}$$

where ε_0 is the vacuum permittivity, V is the volume of pore water, k_B is the Boltzmann constant, and T is the temperature. Var[M] is calculated from <M $^2>$ - <M $>^2$, implying the mean square fluctuation of the total dipole moment.

Water adsorption energy

The adsorption energy of water in the C-S-H pore with water film was calculated through: $E_{\rm ads} = E_{\rm total} - E_{\rm CSH} - nE_{\rm H_2O}$, where $E_{\rm total}$ is the total potential energy of the C-S-H slab with water adsorption. $E_{\rm CSH}$ and $E_{\rm H_2O}$ are the potential energies of the C-S-H slab with water film and a single water molecule, respectively. n is the number of adsorbed water molecules. To record the adsorption energy variation with respect to water surface coverage, the configurations of C-S-H with water adsorption were output every 1 ps (GCMC step). The potential energy at a certain step was then calculated through energy minimization. The water saturation degree is calculated by $N/N_{\rm max}$, where N represents the adsorbed water molar amount in the slits and $N_{\rm max}$ refers to the maximum water that could be adsorbed into the nanopores.

Water orientation distribution

We analyzed the water orientation distribution on C-S-H surfaces with varying Ca/Si ratios. Utilizing C-S-H pore models with a water saturation degree of 0.33 as a representative, the statistical water orientation distribution is illustrated (Supplementary Fig. 12a). This water content ensures a sufficient number of molecules to mitigate randomness in our simulation results while maintaining a layered water state to exclude the effects of capillary condensation. The humid C-S-H models were fully relaxed using minimization and NPT ensembles, after which a 2 ns NVT ensemble at 300 K was utilized to equilibrate the surface water. The atom trajectories were recorded every 1 ps, and the water orientation was calculated every 10 ps, and the average orientation angle in the last 1 ns was employed as the final orientation distribution. Water molecules can interact with the C-S-H surface in two orientations, depending on whether the O_w or H_w atom is closer to the solid surface (Supplementary Fig. 12b). For simplification, we focused on the water molecules at the bottom of the C-S-H slit pores. The orientation

angle (θ) describes the order of water orientation: a positive θ indicates that the H_w atoms face the solid surface, while a negative θ suggests that O_w is closer to the C-S-H surface.

Data availability

The data supporting the findings of this study are included within the paper and its Supplementary Information. Source data are provided with this paper.

Code availability

All the software used in this work is open source. No specific code was developed for this work.

References

- Fankhauser, S. et al. The meaning of net zero and how to get it right. Nat. Clim. Change 12, 15–21 (2022).
- Mysiak, J., Surminski, S., Thieken, A., Mechler, R. & Aerts, J. Brief communication: Sendai framework for disaster risk reduction–success or warning sign for Paris? *Nat. Hazards Earth* Syst. Sci. 16, 2189–2193 (2016).
- 3. Romanov, V. et al. Mineralization of carbon dioxide: a literature review. *ChemBioEng Rev.* **2**, 231–256 (2015).
- Gadikota, G. Carbon mineralization pathways for carbon capture, storage and utilization. Commun. Chem. 4, 23 (2021).
- Kelemen, P. B. et al. Engineered carbon mineralization in ultramafic rocks for CO₂ removal from air: review and new insights. *Chem. Geol.* 550, 119628 (2020).
- Pan, S.-Y. et al. CO₂ mineralization and utilization by alkaline solid wastes for potential carbon reduction. *Nat. Sustain.* 3, 399–405 (2020).
- Pan, S.-Y., Chiang, P.-C., Chen, Y.-H., Tan, C.-S. & Chang, E. E. Ex situ CO₂ capture by carbonation of steelmaking slag coupled with metalworking wastewater in a rotating packed bed. *Environ. Sci. Technol.* 47, 3308–3315 (2013).
- Kaliyavaradhan, S. K., Ling, T.-C. & Mo, K. H. Valorization of waste powders from cement-concrete life cycle: a pathway to circular future. J. Clean. Prod. 268, 122358 (2020).
- Ukwattage, N. L., Ranjith, P. G., Yellishetty, M., Bui, H. H. & Xu, T. A laboratory-scale study of the aqueous mineral carbonation of coal fly ash for CO₂ sequestration. J. Clean. Prod. 103, 665–674 (2015).
- Xie, H. et al. Scientific and engineering progress in CO₂ mineralization using industrial waste and natural minerals. *Engineering* 1, 150–157 (2015).
- Poon, C. S., Shen, P., Jiang, Y., Ma, Z. & Xuan, D. Total recycling of concrete waste using accelerated carbonation: a review. *Cem. Concr. Res.* 173, 107284 (2023).
- Abdolhosseini Qomi, M. J. et al. Molecular-scale mechanisms of CO₂ mineralization in nanoscale interfacial water films. Nat. Rev. Chem. 6, 598–613 (2022).
- Xu, Z. et al. Effects of temperature, humidity and CO₂ concentration on carbonation of cement-based materials: a review. Constr. Build. Mater. 346, 128399 (2022).
- Turcry, P., Oksri-Nelfia, L., Younsi, A. & Aït-Mokhtar, A. Analysis of an accelerated carbonation test with severe preconditioning. *Cem. Concr. Res.* 57, 70–78 (2014).
- Morandeau, A., Thiéry, M. & Dangla, P. Investigation of the carbonation mechanism of CH and C-S-H in terms of kinetics, microstructure changes and moisture properties. *Cem. Concr. Res.* 56, 153–170 (2014).
- Hyvert, N., Sellier, A., Duprat, F., Rougeau, P. & Francisco, P. Dependency of C-S-H carbonation rate on CO₂ pressure to explain transition from accelerated tests to natural carbonation. *Cem. Concr. Res.* 40, 1582–1589 (2010).
- Steiner, S., Lothenbach, B., Proske, T., Borgschulte, A. & Winnefeld,
 F. Effect of relative humidity on the carbonation rate of portlandite,

- calcium silicate hydrates and ettringite. Cem. Concr. Res. 135, 106116 (2020).
- Liu, X. et al. Carbonation behavior of calcium silicate hydrate (C-S-H): Its potential for CO₂ capture. Chem. Eng. J. 431, 134243 (2022).
- Santos, R. M. et al. Stabilization of basic oxygen furnace slag by hotstage carbonation treatment. Chem. Eng. J. 203, 239–250 (2012).
- 20. Faucher, S. et al. Critical knowledge gaps in mass transport through single-digit nanopores: a review and perspective. *J. Phys. Chem. C.* **123**, 21309–21326 (2019).
- Zare, S., Uddin, K. S., Funk, A., Miller, Q. R. & Qomi, M. J. A. Nanoconfinement matters in humidified CO₂ interaction with metal silicates. *Environ. Sci. Nano* 9, 3766–3779 (2022).
- Nguyen-Tuan, L. et al. Quantitative study on growth and porosity of C-S-H structures: experiments and simulations. *Cem. Concr. Res.* 174, 107294 (2023).
- 23. Placencia-Gómez, E. et al. Critical water coverage during forsterite carbonation in thin water films: activating dissolution and mass transport. *Environ. Sci. Technol.* **54**, 6888–6899 (2020).
- 24. Li, G. et al. Optimal CO_2 intake in metastable water film in mesoporous materials. *Nat. Commun.* **15**, 10790 (2024).
- 25. Li, G. et al. Water's grip on CO_2 intake in mesopores of dicalcium silicate. Cem. Concr. Res. **192**, 107842 (2025).
- Bonnaud, P., Ji, Q., Coasne, B., Pellenq, R.-M. & Van Vliet, K. Thermodynamics of water confined in porous calcium-silicate-hydrates. Langmuir 28, 11422–11432 (2012).
- Gelb, L. D., Gubbins, K., Radhakrishnan, R. & Sliwinska-Bartkowiak, M. Phase separation in confined systems. *Rep. Prog. Phys.* 62, 1573 (1999).
- 28. Saam, W. & Cole, M. W. Excitations and thermodynamics for liquidhelium films. *Phys. Rev. B* **11**, 1086 (1975).
- de Keizer, A., Michalski, T. & Findenegg, G. H. Fluids in pores: experimental and computer simulation studies of multilayer adsorption, pore condensation and critical-point shifts. *Pure Appl. Chem.* 63, 1495–1502 (1991).
- Tuller, M., Or, D. & Dudley, L. M. Adsorption and capillary condensation in porous media: Liquid retention and interfacial configurations in angular pores. Water Resour. Res. 35, 1949–1964 (1999).
- 31. Lin, X. et al. Changes in water vapor adsorption and water film thickness in clayey materials as a function of relative humidity. *Vadose Zone J.* **19**, e20063 (2020).
- Liu, Y. & Wilcox, J. Molecular simulation studies of CO₂ adsorption by carbon model compounds for carbon capture and sequestration applications. *Environ. Sci. Technol.* 47, 95–101 (2013).
- Zhou, J., Zhang, J., Yang, J., Jin, Z. & Luo, K. H. Mechanisms for kerogen wettability transition from water-wet to CO₂-wet: implications for CO₂ sequestration. *Chem. Eng. J.* 428, 132020 (2022).
- Bernard, E., Yan, Y. & Lothenbach, B. Effective cation exchange capacity of calcium silicate hydrates (CSH). Cem. Concr. Res. 143, 106393 (2021).
- Martins-Costa, M. T. & Ruiz-López, M. F. The structure of carbon dioxide at the air-water interface and its chemical implications. Chemistry 30, e202400825 (2024).
- Bonnaud, P. A., Coasne, B. & Pellenq, R. J. Molecular simulation of water confined in nanoporous silica. *J. Phys. Condens. Matter* 22, 284110 (2010).
- Coasne, B., Grosman, A., Ortega, C. & Pellenq, R. Physisorption in nanopores of various sizes and shapes: a Grand Canonical Monte Carlo simulation study. in *Studies in Surface Science and Catalysis* (Elsevier, 2002).
- 38. Criado, Y. A., Arias, B. & Abanades, J. C. Effect of the carbonation temperature on the CO₂ carrying capacity of CaO. *Ind. Eng. Chem. Res.* **57**, 12595–12599 (2018).
- Ren, M., Shen, P., Tao, Y. & Poon, C. S. Development of highly carbonation-effective calcium silicates (β-C2S): phase evolution,

- microstructure, and carbonation mechanisms. *Cem. Concr. Res.* **181**. 107542 (2024).
- Gao, Y., Jiang, Y., Tao, Y., Shen, P. & Poon, C. S. Accelerated carbonation of recycled concrete aggregate in semi-wet environments: a promising technique for CO₂ utilization. *Cem. Concr. Res.* 180, 107486 (2024).
- Zajac, M., Skibsted, J., Bullerjahn, F. & Skocek, J. Semi-dry carbonation of recycled concrete paste. J. CO2 Util. 63, 102111 (2022).
- Polino, D., Grifoni, E., Rousseau, R., Parrinello, M. & Glezakou, V.-A. How collective phenomena impact CO₂ reactivity and speciation in different media. J. Phys. Chem. A 124, 3963–3975 (2020).
- Wang, X., Conway, W., Burns, R., McCann, N. & Maeder, M. Comprehensive study of the hydration and dehydration reactions of carbon dioxide in aqueous solution. J. Phys. Chem. A 114, 1734–1740 (2010).
- 44. Battocchio, F., Monteiro, P. J. M. & Wenk, H.-R. Rietveld refinement of the structures of 1.0 C-S-H and 1.5 C-S-H. *Cem. Concr. Res.* **42**, 1534–1548 (2012).
- 45. Qomi, M. A. et al. Combinatorial molecular optimization of cement hydrates. *Nat. Commun.* **5**, 1–10 (2014).
- Pellenq, R. J.-M. et al. A realistic molecular model of cement hydrates. Proc. Natl. Acad. Sci. USA 106, 16102–16107 (2009).
- 47. Tao, Y., Gao, Y., Sun, Y., Pellenq, R. J. M. & Poon, C. S. C-S-H decalcification in seawater: the view from the nanoscale. *Cem. Concr. Res.* **175**. 107385 (2024).
- Beaudoin, J. J., Raki, L. & Alizadeh, R. A 29Si MAS NMR study of modified C-S-H nanostructures. Cem. Concr. Compos. 31, 585-590 (2009).
- Brunet, F., Bertani, P., Charpentier, T., Nonat, A. & Virlet, J. Application of 29Si homonuclear and 1H–29Si heteronuclear NMR correlation to structural studies of calcium silicate hydrates. *J. Phys. Chem. B* 108, 15494–15502 (2004).
- Plimpton, S. Fast parallel algorithms for short-range molecular dynamics. J. Comput. Phys. 117, 1–19 (1995).
- 51. Aktulga, H. M., Fogarty, J. C., Pandit, S. A. & Grama, A. Y. Parallel reactive molecular dynamics: numerical methods and algorithmic techniques. *Parallel Comput.* **38**, 245–259 (2012).
- 52. Yeh, I.-C. & Berkowitz, M. L. Ewald summation for systems with slab geometry. *J. Chem. Phys.* **111**, 3155–3162 (1999).
- Rappe, A. K. & Goddard, W. A. III Charge equilibration for molecular dynamics simulations. J. Phys. Chem. 95, 3358–3363 (1991).
- Nakano, A. Parallel multilevel preconditioned conjugate-gradient approach to variable-charge molecular dynamics. *Comput. Phys. Commun.* 104, 59–69 (1997).
- Cygan, R. T., Romanov, V. N. & Myshakin, E. M. Molecular simulation of carbon dioxide capture by montmorillonite using an accurate and flexible force field. *J. Phys. Chem. C.* 116, 13079–13091 (2012).
- 56. Errington, J., Kiyohara, K., Gubbins, K. & Panagiotopoulos, A. Monte Carlo simulation of high-pressure phase equilibria in aqueous systems. *Fluid Ph. Equilib.* **150**, 33–40 (1998).
- Pitman, M. C. & Van Duin, A. C. Dynamics of confined reactive water in smectite clay–zeolite composites. J. Am. Chem. Soc. 134, 3042–3053 (2012).
- 58. Meyers, C. H. & Dusen, M. S. V. The vapor pressure of liquid and solid carbon dioxide. *Bur. Stand. J. Res.* **10**, 381 (1933).
- Simonnin, P., Noetinger, B. T., Nieto-Draghi, C., Marry, V. & Rotenberg, B. Diffusion under confinement: hydrodynamic finite-size effects in simulation. J. Chem. Theory Comput. 13, 2881–2889 (2017).
- Yeh, I.-C. & Hummer, G. System-size dependence of diffusion coefficients and viscosities from molecular dynamics simulations with periodic boundary conditions. *J. Phys. Chem. B* 108, 15873–15879 (2004).
- 61. Humphrey, W., Dalke, A. & Schulten, K. VMD: visual molecular dynamics. *J. Mol. Graph.* **14**, 33–38 (1996).

- Fuentes-Azcatl, R., Mendoza, N. & Alejandre, J. Improved SPC force field of water based on the dielectric constant: SPC/ε. Phys. A Stat. Mech. Appl. 420, 116–123 (2015).
- Gatti, C., Silvi, B. & Colonna, F. Dipole moment of the water molecule in the condensed phase: a periodic Hartree-Fock estimate. Chem. Phys. Lett. 247, 135–141 (1995).
- 64. Asay, D. B. & Kim, S. H. Evolution of the adsorbed water layer structure on silicon oxide at room temperature. *J. Phys. Chem. B* **109**, 16760–16763 (2005).

Acknowledgements

We wish to thank the following funding for supporting our research: The National Key Research and Development Program of China (Grant No. 2024YFF0508300) awarded to Y.T.; The Young Innovative Researcher Award (Grant No. P0057736) awarded to Y.T. by The Hong Kong Polytechnic University.

Author contributions

Y.T. and G.L. conceived the study, performed the simulation, and wrote the manuscript. Y.T. supervised the research project. Y.G., P.S., and X.Q. assisted with the analysis and discussion of the results. R.J.-M.P. and C.S.P. reviewed and revised the manuscript. All authors contributed to the final version of the manuscript.

Competing interests

The authors declare no competing interests.

Additional information

Supplementary information The online version contains supplementary material available at https://doi.org/10.1038/s41467-025-62580-6.

Correspondence and requests for materials should be addressed to Yong Tao.

Peer review information *Nature Communications* thanks Sebastien Kerisit, Yunjian Li, Carlos Nieto-Draghi, and the other, anonymous, reviewer(s) for their contribution to the peer review of this work. A peer review file is available.

Reprints and permissions information is available at http://www.nature.com/reprints

Publisher's note Springer Nature remains neutral with regard to jurisdictional claims in published maps and institutional affiliations.

Open Access This article is licensed under a Creative Commons Attribution-NonCommercial-NoDerivatives 4.0 International License, which permits any non-commercial use, sharing, distribution and reproduction in any medium or format, as long as you give appropriate credit to the original author(s) and the source, provide a link to the Creative Commons licence, and indicate if you modified the licensed material. You do not have permission under this licence to share adapted material derived from this article or parts of it. The images or other third party material in this article are included in the article's Creative Commons licence, unless indicated otherwise in a credit line to the material. If material is not included in the article's Creative Commons licence and your intended use is not permitted by statutory regulation or exceeds the permitted use, you will need to obtain permission directly from the copyright holder. To view a copy of this licence, visit https://creativecommons.org/licenses/by-nc-nd/4.0/.

© The Author(s) 2025